Rust as Electrodes

Deutsche Ausgabe: DOI: 10.1002/ange.201604040
Internationale Ausgabe: DOI: 10.1002/anie.201604040

In Situ Activating Ubiquitous Rust towards Low-Cost, Efficient, Free-Standing, and Recoverable Oxygen Evolution Electrodes

*Haixia Zhong, Jun Wang, Fanlu Meng, and Xinbo Zhang**

Abstract: *Developing effective ways to recycle rusted stainless steel and to promote the sluggish oxygen evolution reaction (OER), associated with water splitting and metal–air batteries, is important for a resource-sustainable and environment-friendly society. Herein, we propose a strategy to enable rusted stainless steel plate to be used as an abundant and low-cost OER catalyst, wherein a hydrothermal combined in situ electrochemical oxidation–reduction cycle (EORC) method is developed to mimic and expedite the corrosion process, and thus activate stainless steel into free-standing OER electrodes. Benefiting from the plentiful electrolyte-accessible Fe/(Ni) oxyhydroxides, high conductivity and mechanical stability, this electrode exhibits remarkable OER performances including low overpotential, fast kinetics, and long-term durability. The slight degradation in current after long-term use can be repaired immediately in situ by an EORC.*

Stainless steels is a ubiquitous material with a wide variety of important applications, such as use in medical devices, automotive parts, jewelry, and cooking utensils, and playing a crucial role in social progress.[1] Although the notorious metallic corrosion is significantly restrained for stainless steel, it cannot be completely avoided especially under environments including high humidity, pressure, temperature, and/or seawater, still resulting in serious deterioration of stainless steel,[1d] and even endangering public and industrial safety. Generally, rusty stainless steel can be reclaimed by either removal of the corrosion layer or sending back to furnace, which is favorable to preserve valuable alloying elements, while suffering from drawbacks, such as high energy- and time-cost and pollution emissions.[1b,c]

Electrochemically splitting of water into hydrogen and oxygen represents a very promising process to address the ever increasing issues of energy crisis and environment pollution.[2] However, its overall efficiency is seriously hindered by the kinetically sluggish oxygen evolution reaction (OER).[3] Currently, the state-of-the-art OER electrocatalysts are RuO_2 and IrO_2, but their scarcity and prohibitive cost still severely constrain their widespread practical applications.[4] In response, numerous transition-metal (Fe, Ni, Co, etc.) based electrocatalysts have been established for their earth abundant nature.[5] Generally, their high electrical resistance can be somewhat mitigated by immobilizing them on glass carbon or other conductive substrates using a polymer binder (e.g. Nafion), but at the expense of greater cost and buried active sites (result in blocked mass/electron transport and lower electrocatalytic activity). Adding insult to injury, the glued catalyst can still easily peel off from the substrates during vigorous gas evolution/bubbling, worsening the stability.[6] Furthermore, the solvent-evaporation to improve the immobilization of the catalysts will leave them in a dehydrated form, resulting in poor wettability and limited accessible active sites.[7–9] Therefore, it is urgently desirable to develop a novel strategy to fabricate, efficient, and free-standing OER electrodes.

Intriguingly, the surface layer of rusty stainless steel mainly consists of Fe oxide/hydroxide, which could theoretically be polished to become a readily available and efficient OER electrocatalyst, especially on combining with Ni.[10] More importantly, the external rusty layers are usually loose and porous, which favors the mass transport required for OER. Furthermore, the prerequisite high conductivity is ensured by the internal uncorroded substrate, affording sufficient electron transfer for the external active species and making it an ideal alternative toward efficient and integrated OER electrode. To date, there has been little reported on applying the rusty stainless steel in catalyzing the OER. Therefore, to "turn waste into treasure", developing a facile, time- and cost-effective strategy to forge the rusty stainless steel into highly efficient OER electrodes is of great importance and still very challenging.

Herein, as a proof-concept experiment, we intentionally rust the stainless steel plate by hydrothermal method to simulate and expedite the process of natural corrosion and directly activate it into robust OER electrode by electrochemical oxidation–reduction cycle (EORC) in alkaline electrolyte, wherein stainless steel plate not only serves as the current collector and structure scaffold, but also affords the sources to form active species. Unexpectedly, the obtained EORC-activated rusty stainless steel plate (SPN50) can be directly used as an OER electrode, exhibiting low overpotential, fast kinetics with small Tafel slope and long-term durability as a result of abundant Fe/(Ni)OOH, high electron conductivity, excellent wettability, and mechanical stability. Furthermore, the slightly decreased catalytic activity after long-term cycles can be immediately recovered by another EORC in the same electrolyte, benefiting for reutilizing the electrode. And other kinds of artificially rusty stainless steel

[*] H.-x. Zhong, J. Wang, F.-l. Meng, Prof. Dr. X.-b. Zhang
State Key Laboratory of Rare Earth Resource Utilization, Changchun Institute of Applied Chemistry, Chinese Academy of Sciences
Changchun, 130022 (P. R. China)
E-mail: xbzhang@ciac.ac.cn
H.-x. Zhong
University of Chinese Academy of Sciences
Beijing, 100049 (China)
Supporting information and the ORCID identification number(s) for the author(s) of this article can be found under http://dx.doi.org/10.1002/anie.201604040.

plate and naturally rusty stainless steel spoon (RS), lid (RL), and plate (RP), battery case (RBC), as well as Fe rod (FeR) without or with EORC also exhibit superior OER performances.

The fabrication process of SPN50 is schematically shown in Figure 1 a–c. Briefly, newly washed stainless steel plate is converted into corroded stainless steel plate (SPN) by a facile hydrothermal treatment in ammonium solution. Along with this process, the color of the stainless steel plate is changed from grey to olive, indicating the successful growth of the rusty layer. As the atom force microscopy (AFM) images and scanning electron microscopy (SEM) images displayed, the surface of the corroded stainless steel plate is close-packed with uneven particles with average size of 175 nm, quite different from the smooth surface of stainless steel plate (Figure 1 a,b,d,e and Figure S1 in the Supporting Information). And the XRD pattern and Raman spectra identify that the particles are mainly consisted of Fe/(Ni) oxide/hydroxide (Figure S2–3).[11] It is worth noting that the surface of these particles is quite smooth (Figure 1 h). Subsequently, electrochemical oxidation-reduction cycling of corroded stainless steel plate is undertaken to synthesize EORC-activated rusty stainless steel plate (SPN50) in 1 M KOH solution. As shown in Figure 1 f and Figure S1, varisized particles are densely grown on the surface of EORC-activated rusty stainless steel plate, in accompany with the decrease of average size (122 nm) and rougher surfaces in comparison with those of corroded stainless steel plate, due to the in situ partial consumption of the smooth particle and growth of hierarchical nanosheets along its surface via EORC. As the Raman spectra and XRD patterns further verified, the superficial nanosheets induced by EORC are mainly composed of Fe/(Ni)OOH (Figure S2–3), which is well-known as an excellent electrocatalyst toward OER.[2a,11b,d,12] Similarly, the stainless steel plate, treated with EORC, denoted as SP50, is also endowed with dense cross-linked Fe/(Ni)OOH nanosheets on the surface (Figure 1 g and S5 a). And the TEM images of EORC-activated rusty stainless steel plate further reveal the successful formation interconnected nanosheet on the particles (Figure 1 i). Accordingly, the HRTEM images show that distinct lattice spacing (0.22, 0.25, and 0.268 nm) is indexed to (101) plane of $(Ni_{0.67}Fe_{0.33})OOH$, (211) and (400) plane of FeOOH, respectively.

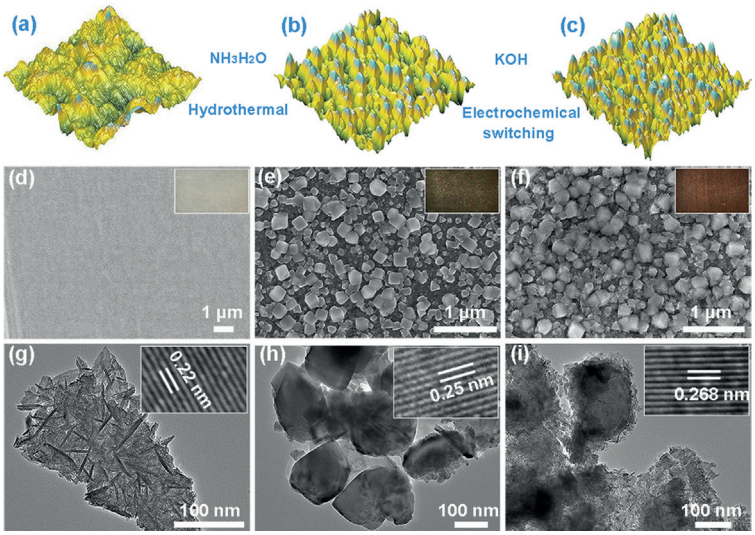

Figure 1. a)–c) schematic fabrication process of rusty stainless steel plate. 3D AFM images of stainless steel plate (a), corroded stainless steel plate (b), and EORC-activated rusty stainless steel plate (c); SEM images of stainless steel plate (d), corroded stainless steel plate (e), and EORC-activated rusty stainless steel plate (f) (inset: the corresponding photographs); TEM images of the particles on EORC-activated stainless steel plate (SP50) (g), corroded stainless steel plate (h) and EORC-activated rusty stainless steel plate (i) (inset: the corresponding HRTEM images).

The HAADF-STEM image of EORC-activated rusty stainless steel plate further confirms the rough surface of the particles, in accordance with SEM results (Figure 2 a,f). And the corresponding element mapping images (Figure 2 b–d, S4 and S5) show that Fe, Ni, and O are homogeneously distributed on the overall particle/nanosheet structure of EORC-activated stainless steel plate, corroded stainless steel plate and EORC-activated rusty stainless steel plate. To further investigate the chemical state of the surface of the rusty stainless steel plate, X-ray photoelectron spectroscopy (XPS) measurement is performed. The presence of Fe, Ni, Cr, and O is confirmed by the survey spectra (Figure S6 and Table S1). And the high resolution Fe $2p_{3/2}$ spectra can be deconvoluted into four types, assigned to Fe (706.5 eV), FeO (709.8 eV), Fe_2O_3 (710.6 eV), and FeOOH (711.5 eV, Figure 2 h).[13] As for Ni $2p_{3/2}$, three fitted peaks located at 852.6, 854.7 and 855.5 eV are ascribed to metallic Ni, NiO, and NiOOH/$Ni(OH)_2$, respectively, while the peaks located at 863.2 eV belongs to the satellite peaks.[14] In addition, the metallic Fe and Ni peaks of EORC-activated stainless steel plate, corroded stainless steel plate, and EORC-activated rusty stainless steel plate have almost disappeared due to the successful generation of dense metal oxides and hydroxides (Figure 2 h,i). Moreover, higher contents of FeOOH and NiOOH are harvested by EORC-activated rusty stainless steel plate in comparison with those of EORC-activated stainless steel plate, corroded stainless steel plate, stainless steel plate (Figure S8 a, b), which predominantly accounts for the higher OER performance (see below). The fitted peaks of the O1s spectrum corresponded to O^{2-} (529.7 eV), OH^- (531 eV), and physical adsorption of water (H_2O, 531.8 eV), respectively.[15] Moreover, EORC-activated rusty stainless steel plate, having a higher percentage of OH^-, holds the apparent advantage of wettability over stainless steel plate, EORC-activated stainless steel plate and corroded stainless steel plate, highlighting its superior in electrolyte penetration (Figure S8 c). To directly elucidate the wettability of the samples, the contact angle of EORC-activated rusty stainless steel plate is determined. As shown in Figure 2 e,f,g and Figure S9, EORC-activated rusty stainless steel plate has the smallest average contact angle (0°) in comparison with corroded stainless steel plate (19.2°), EORC-activated stain-

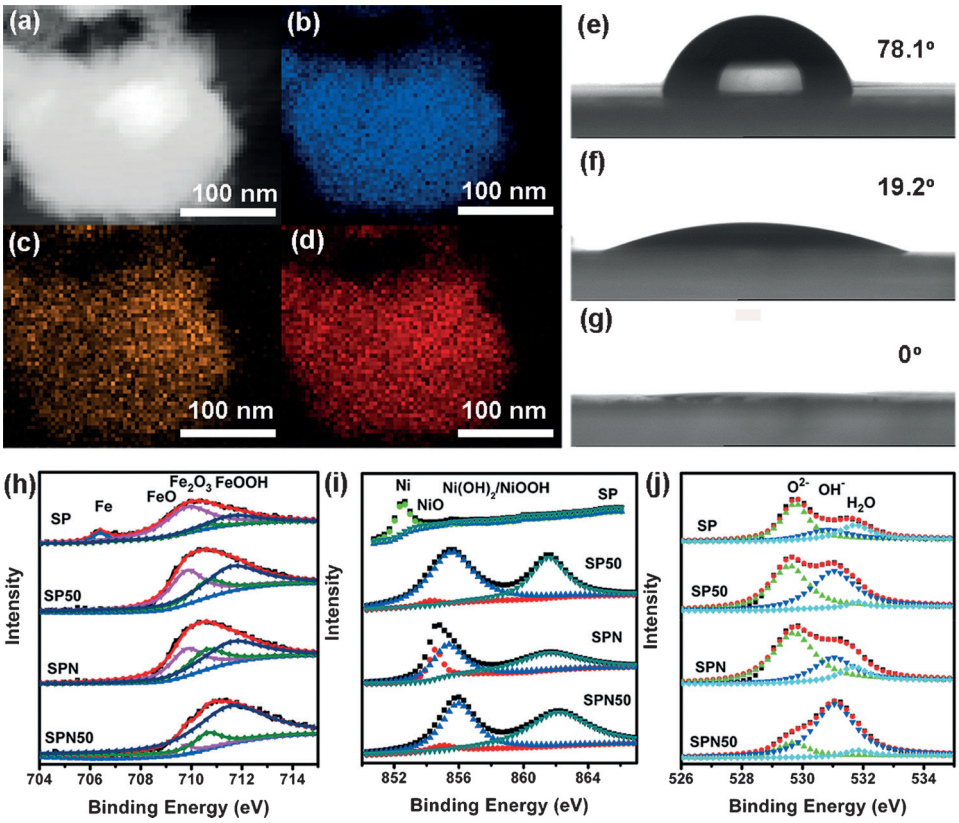

Figure 2. a) STEM image of the particles of EORC-activated rusty stainless steel plate; The corresponding element mapping images of Fe (b), Ni (c), and O (d); Contact angle images of stainless steel plate (e), corroded stainless steel plate (f), and EORC-activated rusty stainless steel plate (g); XPS spectra of Fe $2p_{3/2}$ (h), Ni $2p_{3/2}$ (i) and O 1s (j) of stainless steel plate (SP), EORC-activated stainless steel plate SP50, corroded stainless steel plate (SPN), and EORC-activated rusty stainless steel plate (SPN50).

less steel plate (13.2°), and stainless steel plate (78.1°), demonstrating its excellent wettability and much easier access of the aqueous electrolyte to the active sites.[7c]

The electrocatalytic OER activity of the as-synthesized electrodes in alkaline solution is evaluated in a three-electrode electrochemical cell. The rusty stainless steel plate electrode is directly used as the working electrode, meanwhile a saturated calomel electrode (SCE) and Pt mesh are used as reference electrode and counter electrode, respectively. For comparison, the OER performance of commercial RuO_2 deposited on carbon paper is also tested. The OER polarization curves in Figure 3a reveal that both corroded stainless steel plate and EORC-activated stainless steel plate display greater current densities and lower overpotentials of 0.28 and 0.29 V to reach the benchmarking current density of 10 mA cm^{-2}, respectively, in comparison to stainless steel plate (0.33 V), suggesting that the introduction of Fe/(Ni) oxide and/or hydroxide via the hydrothermal and electrochemical activation plays important role in enhancing the electrocatalytic activity toward OER. Remarkably, the electron resistivity of corroded stainless steel plate and EORC-activated stainless steel plate are low (0.07 and 0.08 mΩ cm) albeit with the growth of various particles, respectively, completely inheriting the high conductivity of SP (0.07 mΩ cm) and ensuring fast electron transfer kinetics for OER. Compared to corroded stainless steel plate and EORC-activated stainless steel plate, EORC-activated rusty stainless steel plate achieves much smaller overpotential (0.26 V, Figure 3a and Table S3), which even outperforms the state-of-the-art RuO_2 (0.32 V). The effective improvement of OER performance at the EORC-activated rusty stainless steel plate electrode is associated with easy electrolyte penetration, intimate contact between the active site and current collector, and the increased active sites, as well as the low electron resistance (0.07 mΩ cm). Note that the OER performance of Cr foil via the same treatment of EORC-activated rusty stainless steel plate

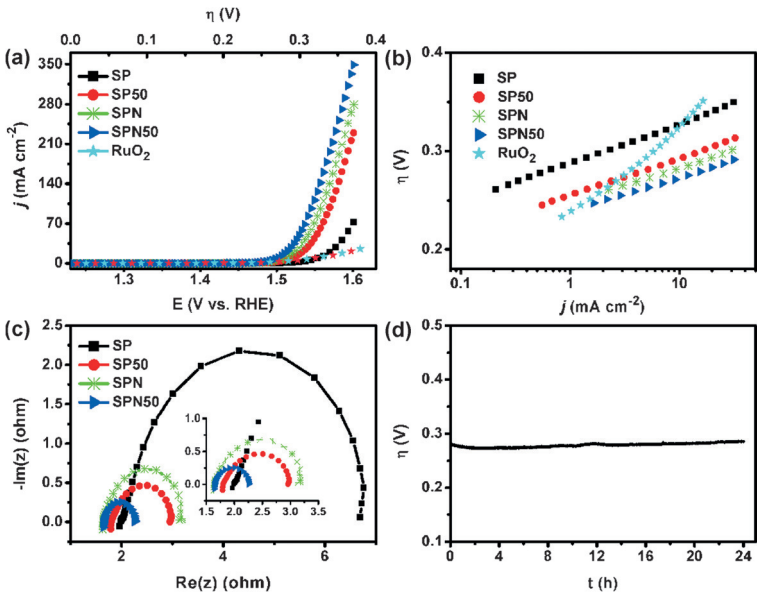

Figure 3. OER polarization curves (a) and Tafel plots (b) of stainless steel plate (SP), EORC-activated stainless steel plate (SP50), corroded stainless steel plate (SPN), EORC-activated rusty stainless steel plate (SPN50), and RuO_2; c) EIS of stainless steel plate (SP), EORC-activated stainless steel plate (SP50), corroded stainless steel plate (SPN), and EORC-activated rusty stainless steel plate (SPN50); d) Chronopotentiometry curve of rusty stainless steel plate in 1 M KOH at a constant current density of 10 mA cm^{-2}.

shows poor OER performance, suggesting the Cr species contribute little to the excellent OER performance at the EORC-activated rusty stainless steel plate electrode (Figure S3a,b and Figure S10). Besides, Fe and Ni foil treating with the identical procedure of EORC-activated rusty stainless steel plate achieve considerable OER performances, indicating the individual Fe and Ni species also contribute to the enhancement of the OER catalytic activity for EORC-activated rusty stainless steel plate (Figure S23). However, they are still lower than that of EORC-activated rusty stainless steel plate, further demonstrating the significant role of the generation of Fe(Ni)OOH in the excellent catalytic activity of EORC-activated rusty stainless steel plate. Furthermore, the surface concentration of redox active Ni centers on the electrode is calculated, which is considered as the real active sites of the Ni based catalyst.[2d] Accordingly, the coverage of redox active Ni centers is 26.6, 9.64, 18.9, and 2.15 nmol cm^{-2} for EORC-activated rusty stainless steel plate, EORC-activated stainless steel plate, corroded stainless steel plate, and stainless steel plate (Figure S11 and Table S3), respectively, consistent with the XPS results. It is thus reasonable to believe that EORC-activated rusty stainless steel plate, possessing higher amounts of real active sites, can obtain higher OER performance in comparison with corroded stainless steel plate, EORC-activated stainless steel plate, and stainless steel plate. Furthermore, the excellent catalytic activity at the EORC-activated rusty stainless steel plate electrode is also gleaned from its good linearity of Tafel plots and smaller Tafel slope (32 mv dec^{-1}) than that of corroded stainless steel plate (34 mv dec^{-1}), EORC-activated stainless steel plate (37 mv dec^{-1}) and stainless steel plate(42 mv dec^{-1}), showing faster OER kinetics.[16] To further gain deep insight into the kinetics during OER process, the electrochemical impedance spectroscopy (EIS) technique is employed. As shown in Figure 3c, lower internal and charge-transfer impedances are observed for EORC-activated rusty stainless steel plate owing to its high electron conductivity ensured by internal uncorroded substrate (Figure S12), suggesting its superior electron-transfer kinetics compared to stainless steel plate, EORC-activated stainless steel plate, and corroded stainless steel plate.[2c,7c,16c] Additionally, the agreement of the theoretical and experimental amount of O_2 suggests that the Faradic efficiency (FE) for EORC-activated rusty stainless steel plate is almost 100% (Figure S13). It is worth noting that the mass activity with large current density (363 mA mg^{-1} at 1.55 V) based on the amount of the surficial Fe/(Ni)OOH particles is harvested by the EORC-activated rusty stainless steel plate electrode (Figure S14c).

To assess the long-term stability of EORC-activated rusty stainless steel plate, both chronopotentiometry and CV scans are performed (Figure 3d and S15). Apparently, the EORC-activated rusty stainless steel plate electrode suffers from little potential degradation over 24 h continuous electrolysis at 10 mA cm^{-2} owing to its stable structure with almost no obvious changes in the morphology and structure indicated by the SEM images, XRD patterns, Raman and XPS spectra (Figure 3d and S16–20). Interestingly, although SPN50 encounters with slight decrease in OER current density after 5000 or 10000 potential cycles due to the gradual consumption of well-defined Fe/(Ni)OOH under large current density and the accumulated gas bubbles, it can be recovered or even improved after another EORC, which is of high importance for reclaiming the electrode in the practical application.

Inspired by the above obtained exciting OER performances, naturally rusted materials as well as other types of artificially surface-corroded stainless steel plate are also used for OER. Interestingly, other kinds of stainless steel plate after hydrothermal corrosion and EORC all give greatly higher OER performance with lower overpotential and smaller Tafel slope as a result of the reduced charge-transfer resistance and increased active sites in comparison with the original ones (Figure S22–25, Table S3), further indicating the feasibility of electrochemically catalyzing OER at rusty stainless steel electrodes. Particularly, the naturally rusty RP, RS, RL and RBC all achieve good OER performance with relatively low onset potential and small Tafel slope (Figure 4 and Table S4). It is thus clear that the rusty stainless steel can be also used as active OER electrode. Furthermore, along with activating by EORC, the color of the rusty parts is changed to brown (Figure 4). Interestingly, more negative onset potential and smaller Tafel slope are gained by the activated ones because of the improved capacity of electron-charge transfer and increased active sites (Figure 4 and Figure S25). Therefore, the rusty metal electrodes can be effectively recycled and given new birth to the application in water electrolysis industry, highlighting the utility value of this stratagem.

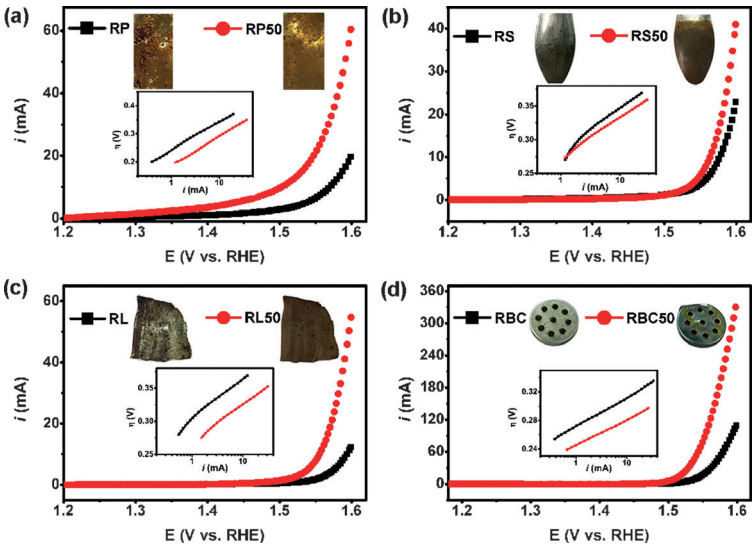

Figure 4. a)–d) OER polarization curves of plate (RP), rusty plate (RP50), spoon (RS), rusty spoon (RS50), lid (RL), rusty lid (RL50), battery case (RBC) and rusty battery case (RBC50) in 1 M KOH (Inset: their corresponding Tafel plots and photographs).

In summary, to turn waste into treasure, we first develop and demonstrate a facile while time- and cost-effective strategy to effectively turn rusty stainless steel into robust, low-cost and free-standing OER electrode. Unexpectedly, the characteristics including high conductivity, superior wettability, superficial Fe/(Ni)OOH, and stable structure boost the excellent OER catalytic activity with large current density, low overpotential, small Tafel slope, and long-term durability at the EORC-activated rusty stainless steel electrode. Furthermore, this electrode can be recovered in situ since its slight anode current attenuation after long term operation can be in situ immediately recovered by another EORC. It should be noted that the naturally rusty stainless steel materials and surface-corroded Fe rod can be successfully recycled to catalyze the OER effectively especially with the help of EORC. The proposed activation and recycle strategy as well as the obtained very promising OER performances would open new avenue for the recycle rusty stainless steel toward new value-added applications, which are of great importance to assist the efforts to build a resource sustainable and environment friendly society.

Acknowledgements

This work is supported by the National Program on Key Basic Research Project of China (973 Program, grant no. 2014CB932300 and 2012CB215500), and the National Natural Science Foundation of China (grant no. 21422108, 51472232, and 51301160).

Keywords: corrosion · electrocatalysts · iron · oxygen evolution reaction · rust

How to cite: *Angew. Chem. Int. Ed.* **2016**, *55*, 9937–9941
Angew. Chem. **2016**, *128*, 10091–10095

[1] a) K. H. Lo, C. H. Shek, J. K. L. Lai, *Mater. Sci. Eng. R* **2009**, *65*, 39; b) B. K. Reck, M. Chambon, S. Hashimoto, T. E. Graedel, *Environ. Sci. Technol.* **2010**, *44*, 3940; c) X. Zhang, X. Hong, *Resour. Conserv. Recycl.* **2011**, *55*, 745; d) K G. Budinski, M. K. Budinski, *Engineering Materials: Properties and Selection*, 7th ed., Prentice Hall, New York, **2001**.

[2] a) J. Wang, H. X. Zhong, Y. L. Qin, X. B. Zhang, *Angew. Chem. Int. Ed.* **2013**, *52*, 5248; *Angew. Chem.* **2013**, *125*, 5356; b) H. Wang, H. W. Lee, Y. Deng, Z. Lu, P. C. Hsu, Y. Liu, D. Lin, Y. Cui, *Nat. Commun.* **2015**, *6*, 7261; c) S. Li, Y. Wang, S. Peng, L. Zhang, A. M. Al-Enizi, H. Zhang, X. Sun, G. Zheng, *Adv. Energy Mater.* **2015**, 1501661; d) J. Wang, K. Li, H. X. Zhong, D. Xu, Z. L. Wang, Z. Jiang, Z. J. Wu, X. B. Zhang, *Angew. Chem. Int. Ed.* **2015**, *54*, 10530; *Angew. Chem.* **2015**, *127*, 10676.

[3] a) Y. Zhu, W. Zhou, Y. Chen, J. Yu, M. Liu, Z. Shao, *Adv. Mater.* **2015**, *27*, 7150; b) A. Gupta, W. D. Chemelewski, C. Buddie Mullins, J. B. Goodenough, *Adv. Mater.* **2015**, *27*, 6063.

[4] a) W. Sun, Y. Song, X. Gong, L. Cao, J. Yang, *Chem. Sci.* **2015**, *6*, 4993; b) T. Reier, M. Oezaslan, P. Strasser, *ACS Catal.* **2012**, *2*, 1765.

[5] a) M. Gong, Y. Li, H. Wang, Y. Liang, J. Z. Wu, J. Zhou, J. Wang, T. Regier, F. Wei, H. Dai, *J. Am. Chem. Soc.* **2013**, *135*, 8452; b) J. Huang, J. Chen, T. Yao, J. He, S. Jiang, Z. Sun, Q. Liu, W. Cheng, F. Hu, Y. Jiang, Z. Pan, S. Wei, *Angew. Chem. Int. Ed.* **2015**, *54*, 8722; *Angew. Chem.* **2015**, *127*, 8846; c) F. Song, X. Hu, *J. Am. Chem. Soc.* **2014**, *136*, 16481.

[6] V. Viswanathan, K. L. Pickrahn, A. C. Luntz, S. F. Bent, J. K. Norskov, *Nano Lett.* **2014**, *14*, 5853.

[7] a) S. Chen, S.-Z. Qiao, *ACS Nano* **2013**, *7*, 10190; b) T. Y. Ma, J. L. Cao, M. Jaroniec, S. Z. Qiao, *Angew. Chem. Int. Ed.* **2015**, *54*, 4646; *Angew. Chem.* **2015**, *127*, 4729; c) S. Chen, J. Duan, M. Jaroniec, S. Z. Qiao, *Angew. Chem. Int. Ed.* **2013**, *52*, 13567; *Angew. Chem.* **2013**, *125*, 13812.

[8] a) Z. Peng, D. Jia, A. M. Al-Enizi, A. A. Elzatahry, G. Zheng, *Adv. Energy Mater.* **2015**, *5*, 1402031; b) P. Chen, K. Xu, Z. Fang, Y. Tong, J. Wu, X. Lu, X. Peng, H. Ding, C. Wu, Y. Xie, *Angew. Chem. Int. Ed.* **2015**, *54*, 14710; *Angew. Chem.* **2015**, *127*, 14923; c) X. Yu, M. Zhang, J. Chen, Y. Li, G. Shi, *Adv. Energy Mater.* **2016**, *6*, 1501492.

[9] a) X. Lu, C. Zhao, *Nat. Commun.* **2015**, *6*, 6616; b) H. Schäfer, S. Sadaf, L. Walder, K. Kuepper, S. Dinklage, J. Wollschläger, L. Schneider, M. Steinhart, J. Hardege, D. Daum, *Energy Environ. Sci.* **2015**, *8*, 2685; c) H. Schäfer, S. M. Beladi-Mousavi, L. Walder, J. Wollschläger, O. Kuschel, S. Ichilmann, S. Sadaf, M. Steinhart, K. Küpper, L. Schneider, *ACS Catal.* **2015**, *5*, 2671.

[10] a) J. A. Haber, Y. Cai, S. Jung, C. Xiang, S. Mitrovic, J. Jin, A. T. Bell, J. M. Gregoire, *Energy Environ. Sci.* **2014**, *7*, 682; b) A. S. Batchellor, S. W. Boettcher, *ACS Catal.* **2015**, *5*, 6680; c) X. Long, J. Li, S. Xiao, K. Yan, Z. Wang, H. Chen, S. Yang, *Angew. Chem. Int. Ed.* **2014**, *53*, 7584; *Angew. Chem.* **2014**, *126*, 7714.

[11] a) A. Kleiman-Shwarsctein, Y. S. Hu, A. J. Forman, G. D. Stucky, E. W. McFarland, *J. Phys. Chem. C* **2008**, *112*, 15900; b) J. E. Maslar, W. S. Hurst, W. J. Bowers, J. H. Hendricks, M. I. Aquino, *J. Electrochem. Soc.* **2000**, *147*, 2532; c) Y. L. Lo, B. J. Hwang, *Langmuir* **1998**, *14*, 944; d) D. L. A. de Faria, S. Venâncio Silva, M. T. de Oliveira, *J. Raman Spectrosc.* **1997**, *28*, 873; e) J. Ma, J. Lian, X. Duan, X. Liu, W. Zheng, *J. Phys. Chem. C* **2010**, *114*, 10671.

[12] a) W. D. Chemelewski, J. R. Rosenstock, C. B. Mullins, *J. Mater. Chem. A* **2014**, *2*, 14957; b) S. Jiao, L. Xu, K. Hu, J. Li, S. Gao, D. Xu, *J. Phys. Chem. C* **2010**, *114*, 269.

[13] a) R. D. Smith, M. S. Prevot, R. D. Fagan, S. Trudel, C. P. Berlinguette, *J. Am. Chem. Soc.* **2013**, *135*, 11580; b) S. J. Yuan, S. O. Pehkonen, *Colloids Surf. B* **2007**, *59*, 87.

[14] H. Liang, F. Meng, M. Caban-Acevedo, L. Li, A. Forticaux, L. Xiu, Z. Wang, S. Jin, *Nano Lett.* **2015**, *15*, 1421.

[15] P. W. Menezes, A. Indra, D. González-Flores, N. R. Sahraie, I. Zaharieva, M. Schwarze, P. Strasser, H. Dau, M. Driess, *ACS Catal.* **2015**, *5*, 2017.

[16] a) Y. Hou, M. R. Lohe, J. Zhang, S. Liu, X. Zhuang, X. Feng, *Energy Environ. Sci.* **2016**, *9*, 478; b) X. Lu, W. L. Yim, B. H. Suryanto, C. Zhao, *J. Am. Chem. Soc.* **2015**, *137*, 2901; c) C. C. McCrory, S. Jung, J. C. Peters, T. F. Jaramillo, *J. Am. Chem. Soc.* **2013**, *135*, 16977; d) H. Jin, J. Wang, D. Su, Z. Wei, Z. Pang, Y. Wang, *J. Am. Chem. Soc.* **2015**, *137*, 2688.

Received: April 26, 2016
Published online: July 20, 2016

